European Journal of Cell Biology 103 (2024) 151396

Contents lists available at ScienceDirect

European Journal of Cell Biology

journal homepage: www.elsevier.com/locate/ejcb

Physico-chemical characterization of the tumour microenvironment of pancreatic ductal adenocarcinoma

Elena García-Gareta [a,b,c,*], Alejandro Calderón-Villalba [a], Pilar Alamán-Díez [a], Carlos Gracia Costa [a], Pedro Enrique Guerrero [a], Carlota Mur [d], Ana Rueda Flores [a], Nerea Olivera Jurjo [a], Patricia Sancho [b], María Ángeles Pérez [a,b], José Manuel García-Aznar [a,b]

[a] Multiscale in Mechanical & Biological Engineering Research Group, Aragon Institute of Engineering Research (I3A), School of Engineering & Architecture, University of Zaragoza, Zaragoza, Aragon, Spain
[b] Aragon Institute for Health Research (IIS Aragon), Miguel Servet University Hospital, Zaragoza, Aragon, Spain
[c] Division of Biomaterials & Tissue Engineering, UCL Eastman Dental Institute, University College London, London, United Kingdom
[d] Aragon Institute of Engineering Research (I3A), School of Engineering & Architecture, University of Zaragoza, Zaragoza, Aragon, Spain

ARTICLE INFO

Keywords:
Pancreatic ductal adenocarcinoma
Tumour microenvironment
Xenograft
Biological bioreactor
Physico-chemical properties
Decellularization

ABSTRACT

Pancreatic ductal adenocarcinoma (PDAC) is a highly aggressive lethal malignancy that accounts for more than 90% of pancreatic cancer diagnoses. Our research is focused on the physico-chemical properties of the tumour microenvironment (TME), including its tumoural extracellular matrix (tECM), as they may have an important impact on the success of cancer therapies. PDAC xenografts and their decellularized tECM offer a great material source for research in terms of biomimicry with the original human tumour. Our aim was to evaluate and quantify the physico-chemical properties of the PDAC TME. Both cellularized (native TME) and decellularized (tECM) patient-derived PDAC xenografts were analyzed. A factorial design of experiments identified an optimal combination of factors for effective xenograft decellularization. Our results provide a complete advance in our understanding of the PDAC TME and its corresponding stroma, showing that it presents an interconnected porous architecture with very low permeability and small pores due to the contractility of the cellular components. This fact provides a potential therapeutic strategy based on the therapeutic agent size.

1. Introduction

Pancreatic ductal adenocarcinoma (PDAC) is the most prevalent type of pancreatic neoplasm accounting for more than 90% of pancreatic cancer diagnoses (Schober et al., 2014; Whatcott et al., 2015; Sarantis et al., 2020). PDAC develops in the exocrine compartment of the pancreas and in 2020 became the third leading cause of cancer-related mortality in the United States (Schober et al., 2014; Whatcott et al., 2015; Bengtsson et al., 2020; Sarantis et al., 2020). This is due to late diagnosis as well as the limited response to treatments, which include the classic chemotherapy, surgery and radiotherapy. Although immunotherapies are providing promising and optimistic results in several solid tumours, PDAC displays a non-immunogenic, immune-suppresive and therapy-resistant microenvironment (Sarantis et al., 2020). Understandably, great efforts are being made to defeat this highly aggressive lethal malignancy. These efforts have mainly focused on the individual cancer cells and their genetic mutations leading to their altered behavior. However, in recent years, a paradigm shift occurred and solid tumours started being regarded as organ-like structures or distinct tissues with a tumour microenvironment (TME) comprised of cancerous and non-cancerous cells, growth factors, and a tumoural extracellular matrix (tECM) (Ricci et al., 2013; Winkler et al., 2020; García-Gareta et al., 2022). Particularly, the tECM component of the TME is receiving increasing attention as its importance in tumour development and metastasis is discovered (Henke et al., 2020; García-Gareta et al., 2022).

In PDAC, the characteristic highly dense fibrotic stromal reaction or desmoplasia comprises up to 90% of the tumour volume and constitutes a prominent histological feature of the PDAC TME. The PDAC stroma is heterogeneous and is composed of abundant distinct cell types, as well as acellular components that form a complex and specialized tECM (Feig et al., 2012). Altogether actively contribute to tumour progression, invasion and provide an immunosuppressive microenvironment thanks to

* Corresponding author at: Aragon Institute of Engineering Research (I3A), School of Engineering & Architecture, University of Zaragoza, Zaragoza, Aragon, Spain.
E-mail address: garciage@unizar.es (E. García-Gareta).

https://doi.org/10.1016/j.ejcb.2024.151396
Received 30 August 2023; Received in revised form 25 January 2024; Accepted 10 February 2024
Available online 12 February 2024

a complex crosstalk between the tECM and tumour cells (Feig et al., 2012). Fibrillar collagens and glycosaminoglycans (GAG) are the major components shaping the structure of the tECM (Kim et al., 2021; Tian et al., 2021). However, in our opinion, more research should focus on the TME and its role in response to therapy. Particularly, the physico-chemical properties of the PDAC TME should be investigated as they may have an important impact on the success of different cancer therapies. This physico-chemical characterization could be carried out with an inter-disciplinary approach using cancer biology, tissue engineering and biomaterials science.

Tumour biopsies and their decellularized tECM offer a great source of material for research into the TME in terms of biomimicry, as the original tumour comes from a patient (Hoshiba, 2019; García-Gareta et al., 2022). However, patient consent, ethical approval, and importantly, a limited amount of material are significant hurdles, which may be overcome by using xenotransplantation models (García-Gareta et al., 2022). In these models, patient-derived tumour tissue or cells can be implanted into an immunodeficient animal host, thereby providing a biological bioreactor for the human-derived tissue or cells to function and grow normally (Cozzi et al., 2009; Matossian et al., 2018; Hoffmann et al., 2020). These models allow the growth of an unlimited number of patient-derived tumours. The patient-derived xenografts can then be used whole (intact, native TEM) or decellularized (tECM of the TME) for experimentation (García-Gareta et al., 2022). In order to streamline this research, fast and cost-effective decellularization methods are needed.

Various decellularization methods exist, namely biological (i.e. enzymes), chemical (e.g. surfactants), and physical (e.g. freeze/thaw, ultrasounds) (García-Gareta et al., 2020, 2022). Of all the existing methods, surfactants, either used on their own or most commonly in combination with other methods, have been shown to be very effective at eliminating cellular material, and when used for a minimal and optimized time period, loss or alteration of the ECM is minimized (Gilpin and Yang, 2017). Typically, finding the right combination of decellularization methods is a time-consuming task that could be significantly shortened by carrying out an optimization study that uses factorial design of experiments (DOE), which offers a mathematical tool to develop a multi-factor experimental strategy where all factors and their interactions are systematically investigated (Levin et al., 2018; Kubit et al., 2022). This mathematical tool is routinely utilized to optimize and develop processes in a broad range of industries and scientific fields, such as biopharmaceutical manufacturing, drug discovery, or environmental science (Aldawsari et al., 2022; Hassan et al., 2022; Kubit et al., 2022; Nazim et al., 2022). However, its application in tissue engineering is still limited, although some examples can be seen in the literature (Levin et al., 2018; Malekpour et al., 2021; Sampson et al., 2021; Kulkarni et al., 2022).

The aim of this study was to assess and quantify the physico-chemical properties of the PDAC TME in terms of architecture, permeability, elemental and molecular groups/chemical bonds footprints, which to be best of our knowledge has never been quantified before, to generate valuable information about the TME. This acquired and novel knowledge can then be applied in the collective quest to find effective therapeutic targets for PDAC. To achieve our aim, both cellularized (intact TEM) and decellularized (tECM component of the TEM) patient-derived PDAC xenografts were used. In order to find a rapid and cost-effective method for routine decellularization of patient-derived PDAC xenografts, we applied a factorial DOE ($2^2 \times 3$), where the three factors investigated were varied simultaneously to analyze their interaction and

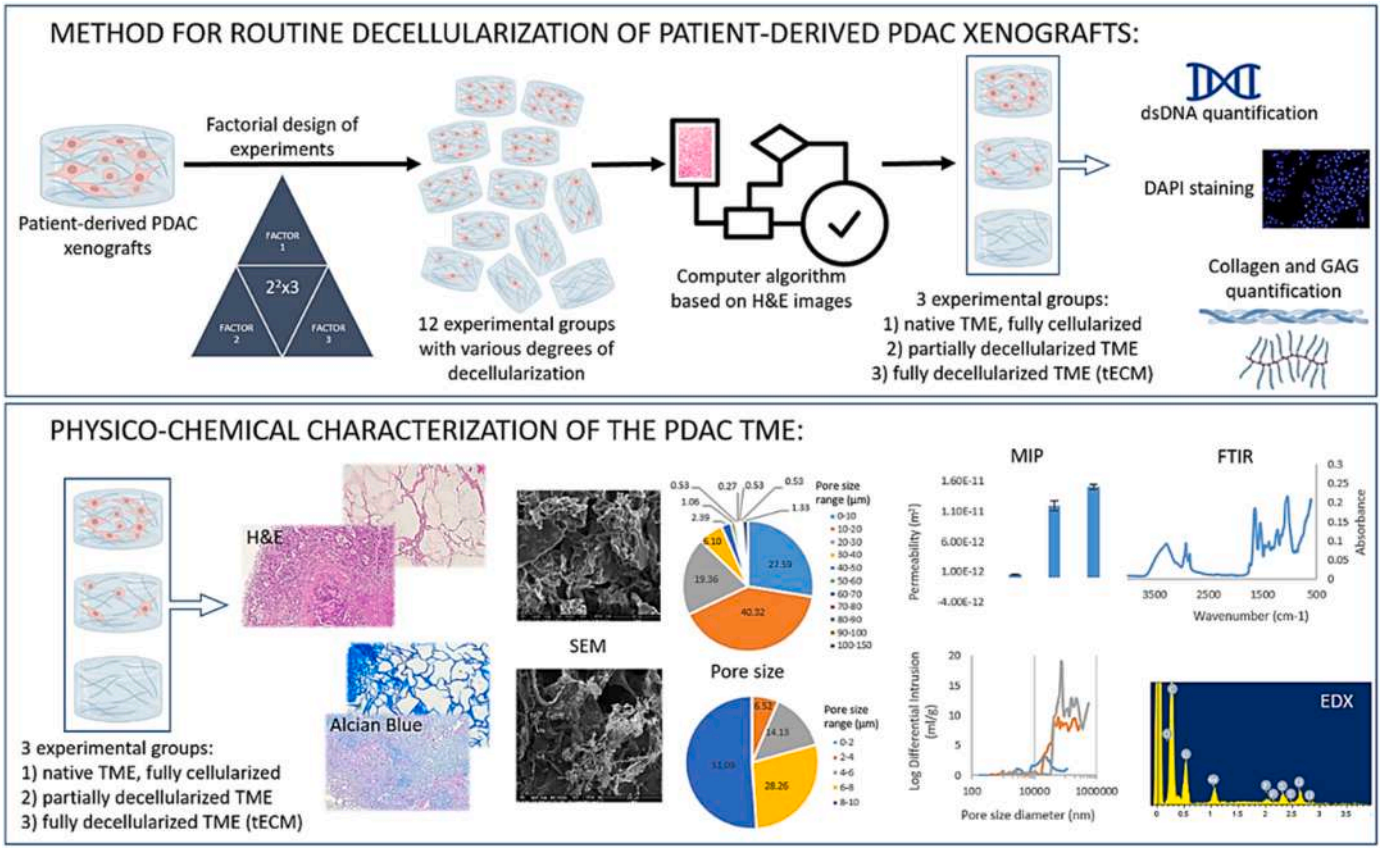

Fig. 1. Visual summary of the experimental work carried out in this study. In the panel at the top, H&E means haematoxylin and eosin staining, dsDNA is double stranded DNA, DAPI is the fluorescent stain 4′,6-diamidino-2-phenylindole, that binds strongly to adenine-thymine-rich regions in dsDNA, and GAG is glycosaminoglycans. In the panel at the bottom, SEM is scanning electron microscopy, MIP is mercury intrusion porosimetry, FTIR is Fourier transform infrared spectroscopy, and EDX is energy dispersive X-ray spectroscopy.

obtain a combination of variables that provide fast, efficient and cost-effective decellularization.

2. Materials and methods

2.1. Experimental summary

Fig. 1 offers a visual summary of the experimental work carried out to achieve the aim of this study. Patient-derived PDAC xenografts were decellularized with a combination of methods that rendered 12 experimental groups when applying a full 2^2x3 factorial design. Assessment of decellularization was done by quantifying the remaining cells using the mandatory Haematoxylin & Eosin (H&E)-stained images and an algorithm. Validation of our quantification method was by dsDNA quantification and staining (using DAPI) of histological sections. For the purpose of validation, we used three experimental groups: 1) native TME, fully cellularized tumours, 2) partially decellularized TME, and 3) fully decellularized TME (tECM). Additionally, we quantified collagen and GAG in the three experimental groups just mentioned.

For physico-chemical characterization of the PDAC TME and its tECM, we performed histological stainings, scanning electron microscopy (SEM), pore size range quantification, total pore area and permeability assessment by mercury intrusion porosimetry (MIP), elemental analysis by energy dispersive X ray analysis (EDX), and molecular groups and chemical bonds analysis by Fourier transform infrared spectroscopy (FTIR). For this purpose, we used the same three experimental groups used in the validation part of our study.

2.2. Patient-derived PDAC xenografts

PDAC-185, PDAC-253 and PDAC-286 patient-derived xenografts (PDX) previously established from different PDAC patients were obtained through the Biobank of the Spanish National Cancer Research Centre (CNIO), Madrid, Spain (reference M-20/002–1). For expansion, tissue fragments from low-passage PDXs were implanted subcutaneously in nude mice (Hsd:Athymic Nude-*Foxn1*^{nu}, Envigo, Spain) and tumour size measured once a week with a calliper. When tumours reached 1 cm^3, the animals were sacrificed, tumours extracted and frozen at − 80 °C (Fig. 2A,B). Mice were housed according to institutional guidelines. All experimental procedures were performed in compliance with the institutional guidelines for the welfare of experimental animals, as approved by the University of Zaragoza Ethics Committee (PI22/17), and in accordance with the guidelines for Ethical Conduct in the Care and Use of Animals, as stated in The International Guiding Principles for Biomedical Research involving Animals, developed by the Council for International Organizations of Medical Sciences (CIOMS). PDAC-253 was used for the first part of this study, whilst PDAC-185 was used for the physico-chemical characterization. Moreover, we performed physical characterization of two additional PDX: PDAC-253 and PDAC-286.

2.3. Factorial design of experiments and experimental groups

In this study, a combination of biological (i.e. protease), chemical (i.e. the surfactant sodium dodecyl sulfate, SDS), and physical (i.e. freeze/thaw and ultrasounds) methods was used. Although more factors could have been used, based on the literature and experience, we chose SDS due to its effectiveness at removing cellular material (Gilpin and Yang, 2017; García-Gareta et al., 2020), ultrasounds to aid SDS penetration into the samples in order to minimize exposure to the surfactant (Syazwani et al., 2015; Manalastas et al., 2021), and a protease to aid in the detachment of cells from the matrix (Gilpin and Yang, 2017; García-Gareta et al., 2020).

Table 1 shows the factorial design where 3 factors were used, namely 1) inclusion of an enzyme, 2) sonication time, and 3) number of sonication plus surfactant cycles. The "sonication time" factor had 3 levels, whilst the other factors had 2 levels each, thus a 2^2x3 factorial design. Since a full factorial design was applied, meaning that all possible

Table 1
Factorial design (2^2x3) used showing the three factors and levels for each factor.

FACTOR	LEVEL
Inclusion of an enzyme	Yes
	No
Sonication time	1 h
	2 h
	4 h
Number of sonication plus surfactant cycles	1
	2

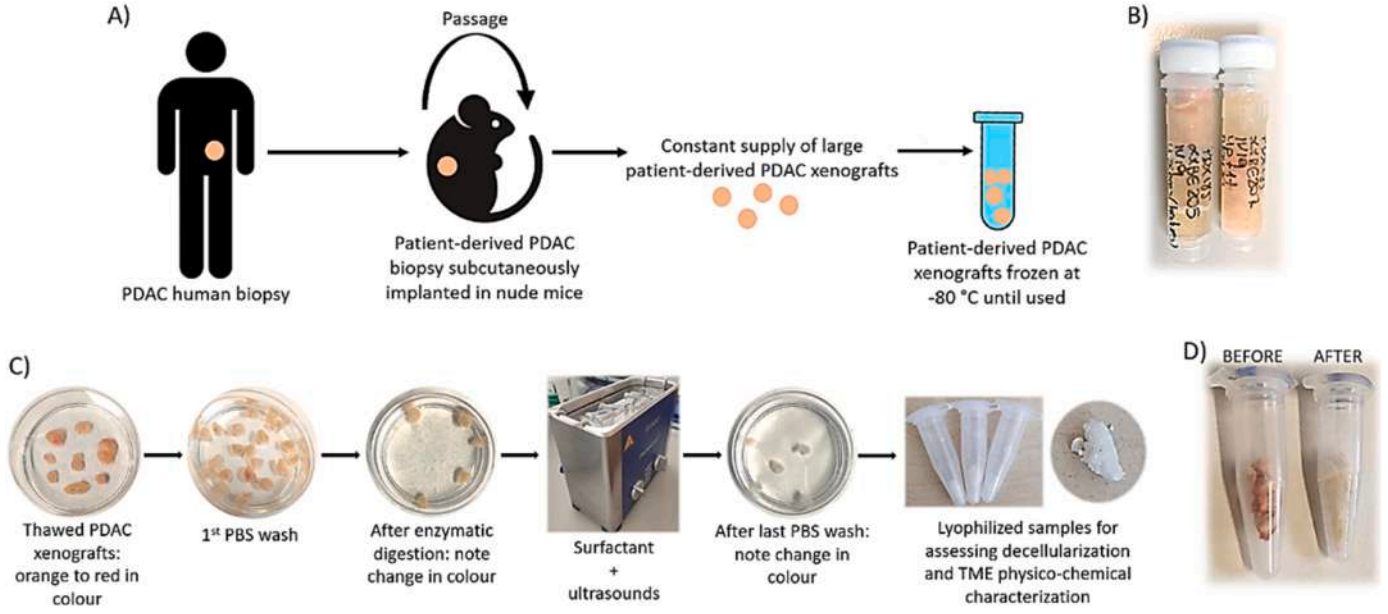

Fig. 2. A) Scheme showing the production of large (~1 cm^3) patient-derived PDAC xenografts used in this study. B) Photo of PDAC xenografts frozen at − 80 °C. C) Stages used for the decellularization process. D) Lyophilized samples before and after decellularization where an evident change in colour is easily observed.

combinations of factors were run, we had 12 experimental groups as detailed in Table 2. All the groups presented an initial freeze/thaw cycle.

2.4. Decellularization process

PDAC xenografts frozen at − 80 °C (Fig. 2B) were thawed to room temperature, cut into pieces of ~5 mm in diameter, and washed in PBS. For those experimental groups where an enzymatic step was used, the xenografts pieces were incubated with the recombinant protease enzyme TrypLE™ Express (12605–010, Gibco, Spain) for 1 h at 37 °C, after which they were washed in PBS. Xenograft pieces were transferred to Eppendorf tubes that were filled with 0.5% SDS (1610301, Biorad, Spain). The tubes were placed in an ultrasonic bath (FB 15047, Fisherbrand™, Fisher Scientific, Spain) and sonicated for 1, 2 or 4 h at 40 KHz. For the experimental groups with a second surfactant plus sonication cycle, the SDS solution was refreshed and the samples sonicated for a further 1 h. Finally, samples were washed in PBS, placed in distilled H_2O at − 80 °C overnight and lyophilised. Fig. 2C offers an overview of the decellularization process.

2.5. Histology and histological stainings

Lyophilised samples were fixed in 4% paraformaldehyde before processing for paraffin histology. Per experimental group, 3 samples were processed, and 8 sections were cut per sample. Half of the sections were stained with H&E, and the other half were stained with Alcian blue. H&E is a classic and principal histological stain in which the haematoxylin stains cell nuclei a purplish blue, and eosin stains the ECM and cytoplasm pink. The histological stain Alcian blue stains acidic polysaccharides such as GAG blue, whilst nuclei and cytoplasm display a red to pink or pale pink color, respectively.

2.6. Quantification of decellularization

H&E images (3 samples per group, 4 images per sample, therefore 12 images per group) were uploaded onto the QuPath 0.3.2 software and the "Cell Detection" algorithm used to count the cells in each image. Results were calculated as cells per area, i.e. cells/mm^2.

2.7. dsDNA quantification

Double stranded DNA (dsDNA) content was quantified with the Hoechst 33–258 kit assay (Sigma-Aldrich) according to the manufacturer's protocol. Lyophilised samples were digested overnight in a solution of collagenase from Clostridium histolyticum (Sigma-Aldrich, 2 mg/ml, 125 CDU/mg) in order to digest the ECM and release the cells.

Table 2
Experimental groups in addition to the control (native TME, fully cellularized PDAC xenografts).

COMMENTS	SONICATION TIME (h)	GROUP NUMBER
- 1 freeze/thaw cycle	1	1
- With enzyme	2	2
- 1 sonication plus surfactant cycle	4	3
- 1 freeze/thaw cycle	1	4
- Without enzyme	2	5
- 1 sonication plus surfactant cycle	4	6
- 1 freeze/thaw cycle	1	7
- With enzyme	2	8
- 2 sonication plus surfactant cycles (second cycle always 1 h)	4	9
- 1 freeze/thaw cycle	1	10
- Without enzyme	2	11
- 2 sonication plus surfactant cycles (second cycle always 1 h)	4	12

The resulting cell suspension was centrifuged at 13,000 rpm for 15 min 100 μl of Hoechst buffer (1 mM EDTA, 10 mM Tris (hydroxymethyl) aminomethane and 0.1 M sodium chloride at pH 7.4, all from Sigma-Aldrich) was added to the pellet. Cells were then lysed by applying three cycles of freezing–thawing (−80 °C), and 20 μl of cell lysate or DNA standards were suspended in 200 μl of Hoechst dye solution (0.1% v/v, Sigma-Aldrich) and added to a black 96-well plate in triplicate. Fluorescence was measured (excitation/emission: 380/440 nm) using a fluorescence spectrophotometer (Synergy HT Multi-mode microplate reader, BioTek Instruments, USA). Readings were converted to DNA content using a standard curve, according to the manufacturer's protocol, with samples containing no cells subtracted as background.

2.8. dsDNA staining

Histological sections were deparaffinized, rehydrated and washed in distilled water before applying DAPI Fluoromount-G® (0100–20, SouthernBiotech, USA) that was left to set for 5 min at room temperature. The sections were cover slipped before imaging with an AxioObserver with ApoTome microscope (Zeiss, Germany).

2.9. Collagen quantification

The collagen content of fresh, partially decellularized and fully decellularized PDAC samples was quantified using the Sircol-2.0 Soluble Collagen Assay Kit (Biocolor, UK) following the manufacturer's instructions. In brief, the samples were digested and collagen was solubilized in a 0.1 mg/ml pepsin (Sigma Aldrich) solution in 0.5 M acetic acid. Extracts were incubated in agitation with Sirius red dye, and absorbance was determined at 556 nm with a microplate reader (Agilent Biotek). Collagen content of each sample was determined using a standard calibration curve, generated using a known concentration of collagen as a standard reference.

2.10. GAG quantification

The sulfated glycosaminoglycan (sGAG) content of fresh, partially decellularized, and fully decellularized PDAC samples was determined using the Blyscan - Sulfated Glycosaminoglycan (sGAG) Assay Kit (Biocolor, UK). In brief, samples weighing between 30 and 50 mg of wet tissue were digested in a 0.1 mg/ml papain solution at 65ºC for 5 h, with intermittent mixing. Subsequently, the samples were stained with 1,9-dimethyl-methylene blue dye reagent, and absorbance was measured at 656 nm using a microplate reader (Agilent Biotek). The total concentration of sGAG in each PDAC sample was calculated from a standard curve derived from various concentrations of bovine tracheal chondroitin-4-sulfate.

2.11. Scanning electron microscopy (SEM) and superficial pore size range

Scanning electron microscopy (SEM) analysis of lyophilized samples used an Inspect TM SEM F50 (FEI Company, US) at 10 kV. Samples were coated with a carbon film before they were examined with the SEM. Superficial pore size range was measured with SEM images (3 images per experimental group) and ImageJ software (National Institute of Health, USA).

2.12. Mercury intrusion porosimetry (MIP)

Pore size distribution, total pore area, and permeability of lyophilized samples was obtained by mercury intrusion porosimetry (MIP, Autopore IV 9500, Micromeritics Inc. USA). This technique measures the intrusion volume of a non-wetting liquid (mercury) in order to calculate data related to the pore structure of the sample. The equipment continuously registers the variation of the mercury intrusion volume inside the sample depending on the pressure applied over the sample.

Pore diameter is calculated with the intrusion pressure, by means of the Washburn equation. The whole intrusion and retraction program was designed to record the mercury volume and the pressure in the range of 1 to 140 μm pore diameters.

2.13. Energy dispersive X-ray spectroscopy (EDX)

Elemental analysis of the carbon-coated samples was studied from the EDX spectra that were obtained at 10 kV using the Inspect TM SEM F50 (FEI Company, US).

2.14. Fourier transform infrared spectroscopy (FTIR)

The molecular groups in the samples were assessed by attenuated total reflectance (ATR) FTIR (VERTEX 70, Bruker, US) over a range of 4000–600 cm^{-1} with a resolution of 2 cm^{-1}. The absorption peaks and frequencies of specific chemical groups were detected by FTIR.

2.15. Data and statistical analysis

The following software packages were used for data and statistical analysis of results: Microsoft Excel 365, Minitab 21.0, and SigmaStat 4.0. For the factorial design data, a statistical regression analysis of variance was carried out where a *p value* below 0.05 was considered a significant result. For dsDNA, collagen, and GAG quantification, total pore area, and permeability, comparisons between groups were made using one-way analysis of variance with a Holm–Sidak post hoc analysis. A *p value* below 0.05 was considered a significant result.

3. Results

3.1. Visual monitoring of the decellularization process

As it can be seen from Fig. 2C, the pieces of xenografts were orange to red in colour at the beginning of the decellularization process. As this advanced, the samples gradually turned white indicating gradual elimination of cellular material (Lü et al., 2014). Fig. 2D shows the

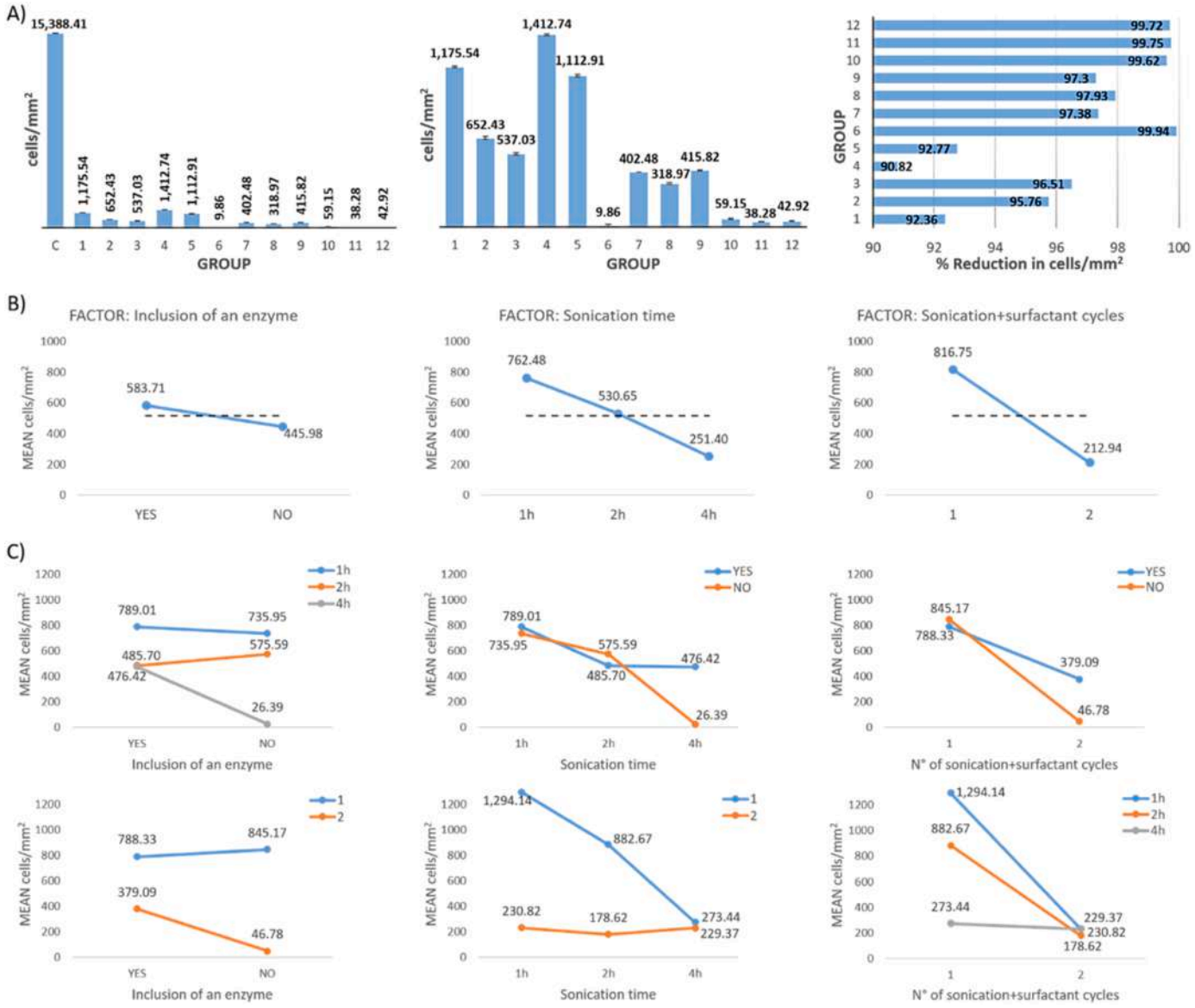

Fig. 3. Data for quantification of decellularization using an algorithm. A) Bar graphs showing cells/mm^2 (C=control or native TME, fully cellularized samples). The second graph does not contain the data for the control to appreciate the differences between the experimental groups. Results show mean ± standard error mean. The last bar graph on the right shows the percentage in reduction in cells/mm^2 compared with the control. B) Main effect plots. C) Two-factor interaction plots.

comparison between lyophilized samples before and after decellularization, showing an evident change in colour. It is worth noting that in all experimental groups decellularized samples seemed quite similar in appearance, so it would not be possible to select which group/s were successfully decellularized simply by visual observation.

3.2. Quantification of decellularization

In this study, we calculated the number of cells per area (mm^2) remaining after the decellularization process. Remarkably, 15,388.41 ± 11.23 cells/mm^2 (mean ± standard error mean) were calculated for the control, showing a very high cellular density present in the PDAC TME (Fig. 3A). As it can be seen from Fig. 3A, a significant reduction in cells per area was observed after decellularization, with a minimum of a 90.82% calculated for Group 4, up to a 99.94% reduction seen for Group 6, which appeared as the most successful experimental group with 9.86 ± 1.00 cells/mm^2 (mean ± standard error mean) left after decellularization. Based on these results, Group 6 was chosen as our fully decellularized TEM (tECM) group, whilst Group 4 was chosen as our partially decellularized TME group.

Main effect plots (Fig. 3B) showed a strong positive effect on cell elimination for sonication time and number of sonication plus surfactant cycles ($p = 0.003$ and $p = 0.001$ respectively, Table 3). Inclusion of an enzyme did not have a significant effect on cell elimination ($p = 0.163$, Table 3), although a negative trend towards including it in the process could be observed (Fig. 3B). Combining the use of an enzyme with longer sonication times or a second sonication plus surfactant cycle (Fig. 3C) improved cell elimination. However, these interactions were not found to be significant (Table 3). On the other hand, the interaction of the other two factors, namely sonication time and number of sonication plus surfactant cycles, was significant ($p = 0.011$, Table 3).

3.3. dsDNA quantification and staining

Quantification of dsDNA showed a significant reduction in dsDNA content between the native TME and the partial (Group 4) and full decellularization (Group 6) groups (Fig. 4A). This analysis showed an 85.48% reduction in dsDNA compared with the 99.94% reduction in cells/mm^2 for Group 6, and a 72.30% dsDNA reduction in comparison to a 90.82% reduction in cells/mm^2 for Group 4. The dsDNA quantification kit used measures dsDNA in cells as well as residual dsDNA trapped in the tECM after decellularization, which may account for the difference in percentages.

Despite some residual auto-fluorescence from the matrix, a reduction in cells could be clearly observed (Fig. 4B). Some blue fluorescence could be seen in the fully decellularized group (Fig. 4B, right image for this group) which may indicate cellular debris or trapped dsDNA in the matrix, as also indicated by the dsDNA quantification analysis.

3.4. Collagen quantification

Quantification of total collagen (Fig. 4C) showed a significant reduction in the amount of soluble collagen, whilst the amount of insoluble collagen slightly increased as the TME was decellularized. Soluble collagen is recently synthesized, not heavily crosslinked, immature collagen, which has not been incorporated into the ECM. Therefore, this collagen is soluble upon immersion in neutral salt solutions like PBS (Minafra et al., 1975). Our results show that a portion soluble collagen is lost during the decellularization process, but a significant amount remains. Insoluble collagen, which is incorporated into the matrix, was kept during the decellularization process.

3.5. GAG quantification

Our results showed a significant reduction of GAG after decellularization (Fig. 4D), which was expected as a large portion of GAG is associated to the cell membrane and therefore, the loss is intrinsic to the decellularization process. Nevertheless, 78.86% of GAG was retained.

3.6. Histological stainings

Histological stainings (Fig. 5) displayed abundant desmoplasia with extensive protein deposition recapitulating the pattern found in human PDAC TME. The native TME was very dense with a high number of cells populating the tECM throughout. The tECM appeared less dense at the edges. Nevertheless, pores could be observed throughout the TME. As the cells were eliminated, the TME opened and pores of different sizes started to be appreciated across the samples. A heterogeneity in terms of tECM morphology was observed for the samples, with denser areas and pores of various sizes. The Alcian blue staining (Fig. 5B) revealed the high GAG content of the tECM as well as its retention during the decellularization process, as already shown in Fig. 4D.

3.7. Architecture and superficial pore size range

Results in Fig. 6 show that the TME is a porous structure, as already shown with the histological stainings, and cells form a thick and dense continuous coating over the tECM, working as a whole network. As the cells are eliminated, residual or accumulated stresses are released, which allows distinguishing features from the tECM such as fibres and further pores. Cellular remains in the partially decellularized TME group could be observed and white arrows point to some examples. Supplementary Figs. S1 and S2 show results for two additional PDX (PDAC-253 and PDAC-286) with similar observations.

Quantification of superficial pore size using SEM images (Fig. 7A) revealed that the native TME presents an 89.17% of pores in the 0–10 μm range, followed by a 9.58% of pores in the 10–20 μm and 1.25% in the 20–30 μm ranges, respectively. Quantitative analysis confirmed that as the cellular component of the TME is eliminated the pores open, and in the fully decellularized TME group only 27.59% of

Table 3
Statistical regression analysis of variance. *Denotes a significant effect or interaction.

Source	Degree of freedom (DF)	Adjusted sums of squares (Adj SS)	Adjusted mean squares (Adj MS)	F-value	P-value
Regression	6	2420501	403417	11.68	0.008 *
Sonication time (h)	1	1051767	1051767	30.46	0.003 *
Inclusion of an enzyme	1	92349	92349	2.67	0.163
2 sonication+surfactant cycles	1	1375291	1375291	39.83	0.001 *
Sonication time (h) & enzyme	1	107799	107799	3.12	0.137
Sonication time (h) & 2 cycles	1	534258	534258	15.47	0.011 *
Enzyme & 2 cycles	1	113573	113573	3.29	0.129
Error	5	172637	34527	-	-
Total	11	2593137	-	-	-

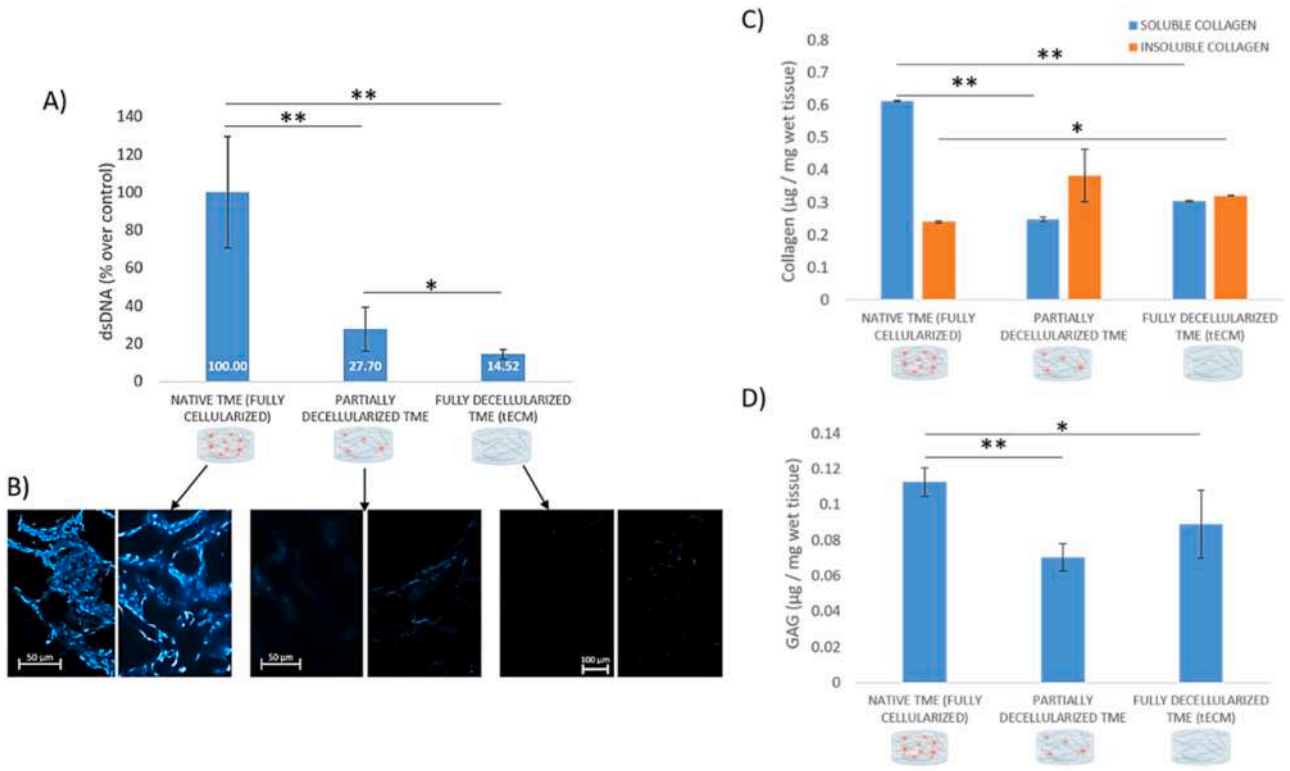

Fig. 4. A) dsDNA quantification. B) dsDNA staining using DAPI of histological sections. C) Collagen quantification. D) GAG quantification. Results show mean ± standard deviation, *$p < 0.05$ and * *$p < 0.001$.

the pores were in the 0 to 10 µm size range, compared with the previously mentioned 89.17% for the native TME. In this sample, the majority of pores were in the 10 to 20 µm size range, and a 1.33% of macro-pores in the 100 to 150 µm size range were calculated. Supplementary Figs. S3A and S4A show the superficial pore size range for the two additional PDX (PDAC-253 and PDAC-286) shown in Figs. S1 and S2. As it can be seen, the results are very similar to those displayed in Fig. 7A, with over 90% of pores in the 0 to 10 µm range for the native TME. Larger pores are seen as the cellular component is eliminated from the TME.

We also studied the distribution of the smallest pores in the 0 to 10 µm size range (Fig. 7B): whilst the majority of pores were in the 2 to 4 and 4 to 6 µm ranges for the native TME and partially decellularized TME samples, for the fully decellularized TME group the majority of pores were found in the 6 to 8 and 8 to 10 µm ranges. Pores in the 6 to 8 µm size range went from 18.22% in the control to 28.26% in the fully decellularized group, and pores in the 8 to 10 µm size range went from 9.35% in the control to 51.09% after complete decellularization. For the fully decellularized TME group, no pores were measured in the 0 to 2 µm size range, in contrast to the other 2 experimental groups, where 3.27% and 20.20% of pores were found in this range for the native TME and partially decellularized TME groups respectively. Regarding the results for the two additional PDX (PDAC-253 and PDAC-286) displayed in Figs. S3B and S4B, pores were measured in the 0 to 2 µm size range for the fully decellularized TME, although the percentage of pores in this size range decreased as the cells were eliminated, as previously observed. We could also see that the percentage of pores in the 8 to 10 µm size range increased after complete decellularization for these two additional PDX.

3.8. Total pore area, permeability and pore size distribution

MIP analysis showed similar pore size distributions (Fig. 8A) to those calculated by SEM images (Fig. 8). For the native TME group, the majority of pores were below 40 µm in diameter, with a large percentage of those below 10 µm. Of those pores between 1 and 10 µm, the majority were in the 2 to 5 µm range. A small fraction of pores were below 1 µm in size. As cells were eliminated larger pores could be measured as well. Calculation of total pore area (Fig. 8B) showed an increase over the native TME group for the partial and fully decellularized TME groups. Finally, permeability increased by two orders of magnitude as the cells were eliminated from the TME (Fig. 8C).

3.9. Elemental footprint

The elemental footprint of a biological sample provides useful information about the chemical elements present in it and whether any mineral formations, i.e. calcifications, may be present. Elemental analysis by EDX (Fig. 9) showed that the most abundant elements present in the spectra were carbon (C) and oxygen (O), which come from the organic molecules that make up the tECM and cellular elements of the TME. C also comes from the C coating applied to the samples. Nitrogen (N) and sulfur (S) are also present in the organic matter of the TME. Additionally, S would come from the dimethyl sulfoxide (DMSO) used to freeze the PDAC xenografts before the decellularization process. For the partial and full decellularization groups, S may also be there as a residual from the SDS. The rest of the elements observed, namely sodium (Na), phosphorus (P), potassium (K) and chlorine (Cl), are present in the composition of PBS (NaCl, KCl, Na_2HPO_4, and KH_2PO_4), which was used to wash the samples. Ca could not be detected suggesting absence of calcifications.

3.10. Molecular groups and chemical bonds footprint

FTIR is a useful technique to investigate the molecular groups and bonds present in a sample, offering a unique chemical footprint for the investigated specimen. FTIR results can be seen in Fig. 10. The peaks/shoulders observed in the spectra correspond to organic molecular

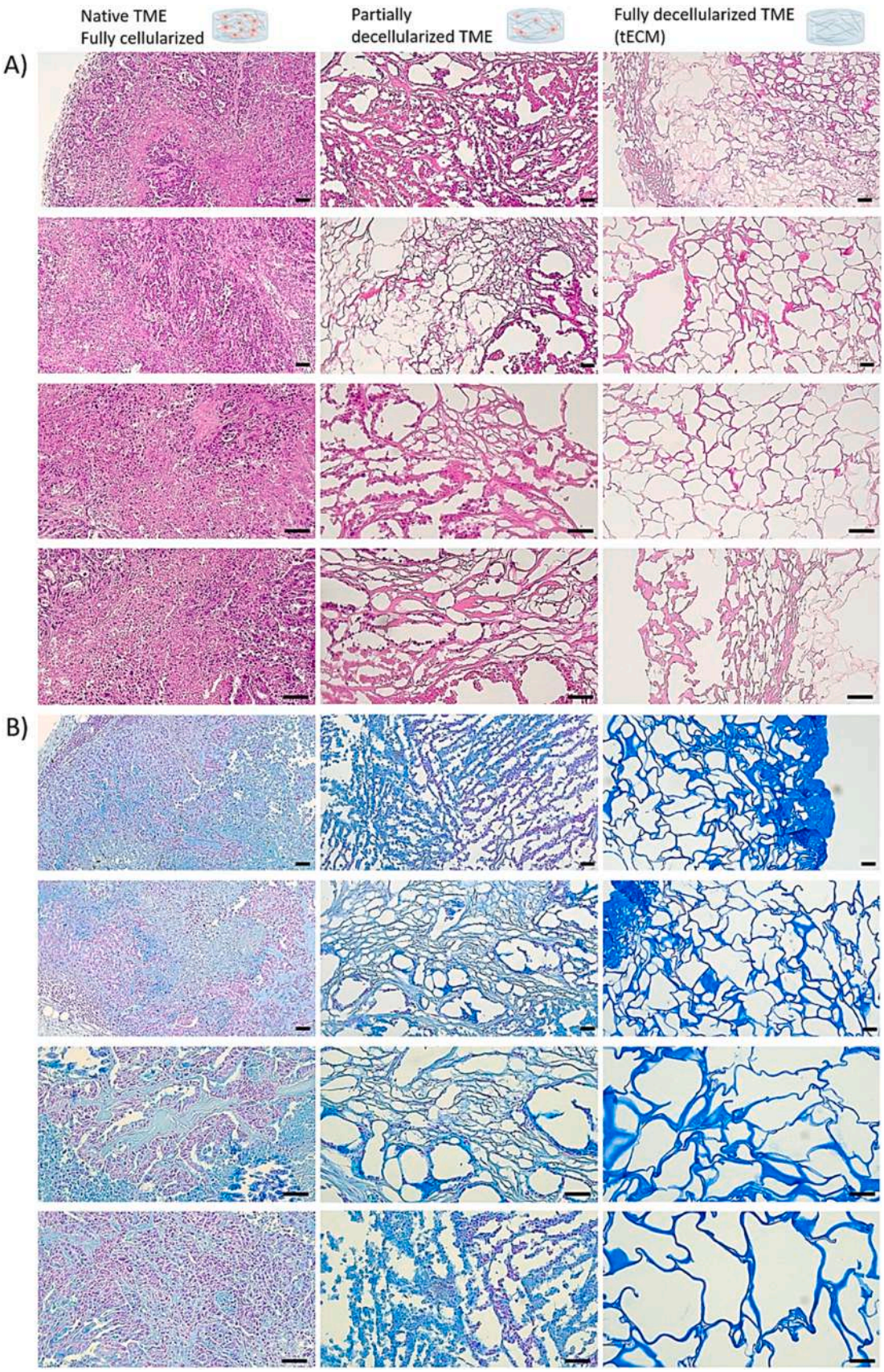

Fig. 5. A) H&E staining (pink=matrix and purple dots=cells) and B) Alcian blue staining (blue=GAG in matrix and pink/purple dots=cells) of the 3 experimental groups used for physico-chemical characterization of the TME using PDAC-185. Scale bar = 100 μm.

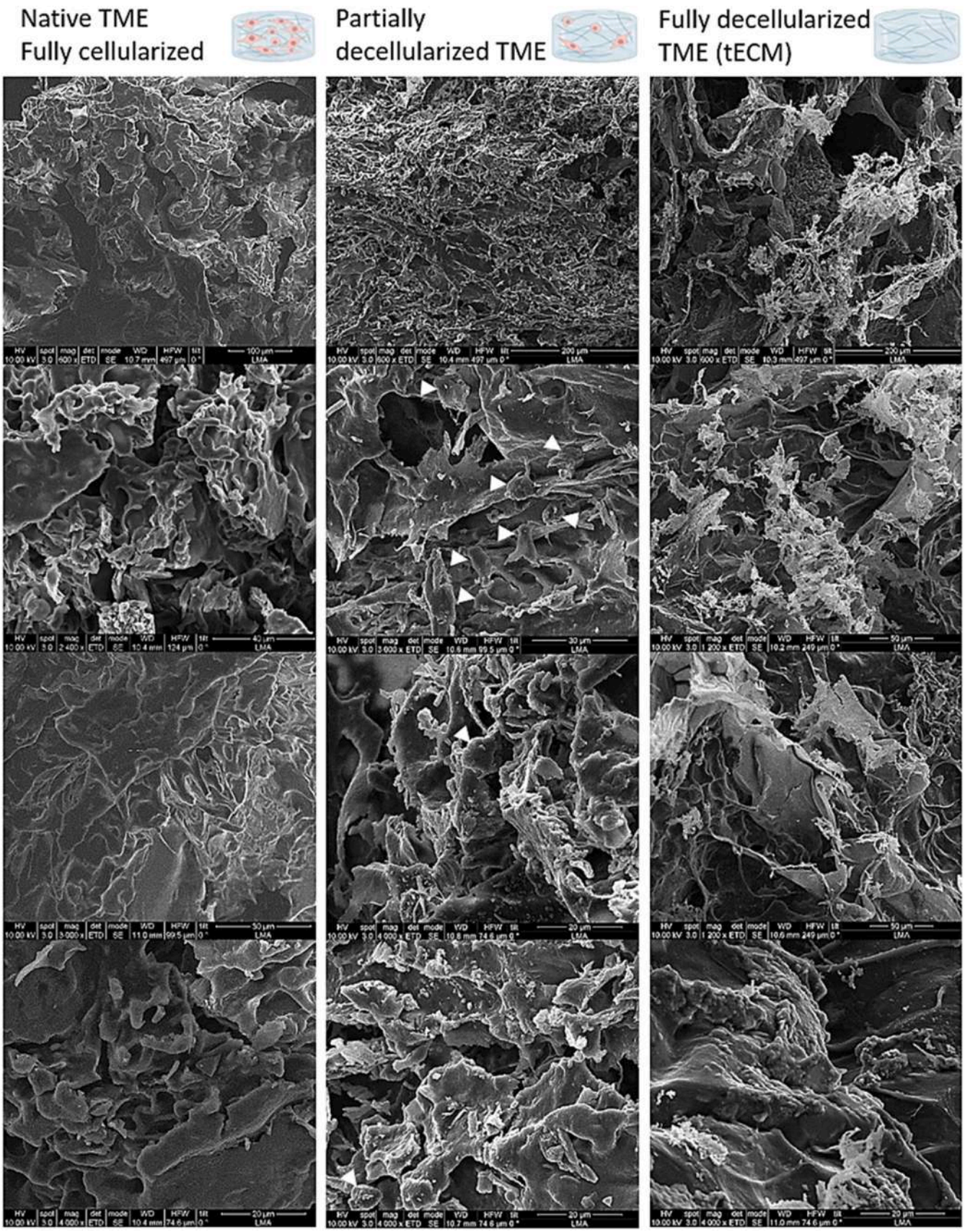

Fig. 6. A) SEM images of the 3 experimental groups used for physico-chemical characterization of the TME using PDAC-185. White arrows point at cellular remains.

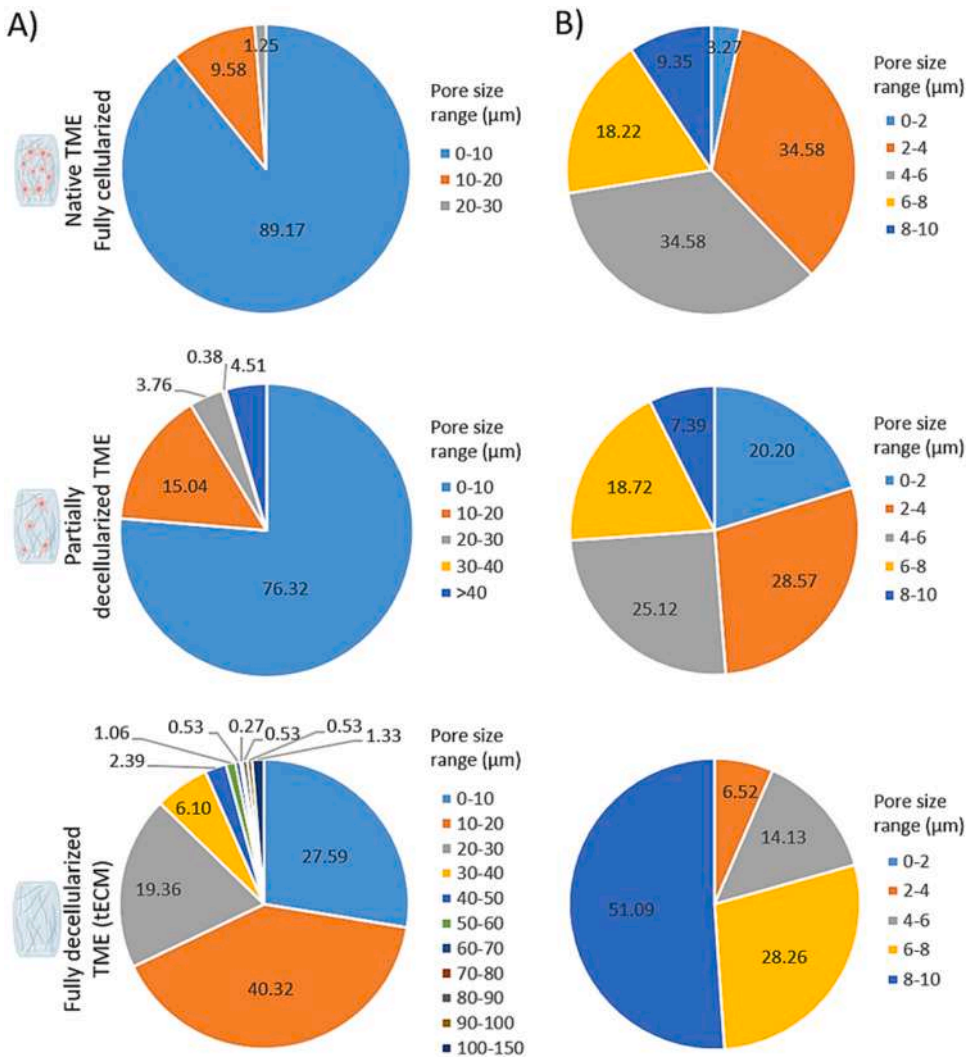

Fig. 7. Superficial pore size analysis based on SEM images of PDAC-185. A) All pores. B) Breakdown of pores in the 0 to 10 µm range.

groups bonds present in proteins, lipids and carbohydrates (Malek et al., 2014; Kumar et al., 2020). As the cells were eliminated from the TEM, new peaks and shoulders appeared, mainly at ~3420 cm^{-1}, which corresponds to the stretch of hydroxyl groups (O-H), and at ~920 to 880 cm^{-1}, which corresponds to the out-of-plane bend of C-H bonds of aromatic groups (Margoshes and Fassel, 1955). New peaks and shoulders could also be seen in the 1640 to 1110 cm^{-1} range of the spectra, corresponding to C═O stretch in amides, N-H bend in amides, C═C stretch of alkene groups, C-H bend of aliphatic groups, and C-O stretch in carbohydrates and proteins. Finally, there was a shoulder only observed in the fully cellularized, native TME group, which corresponds to both the C═O stretch of amide groups and the C═C stretch of alkene groups (marked red bold in Fig. 10).

4. Discussion

PDAC is a highly aggressive lethal malignancy with limited response to the classic treatments of chemotherapy, surgery and radiotherapy (Schober et al., 2014; Whatcott et al., 2015; Sarantis et al., 2020). Besides, PDAC displays a non-immunogenic, immune-suppressive and therapy-resistant microenvironment (Sarantis et al., 2020). Therefore, great efforts are in place to find effective therapeutic regimes for PDAC. In PDAC, desmoplasia is a key factor to understand the disease, representing a source of new therapeutic targets as it contains several potential molecules that could serve as biomarkers. PDAC is one of the largest solid tumours as well as one of the most stroma-rich cancers (Feig et al., 2012). As outlined in the introduction, in our opinion, more research should focus on the physico-chemical characterization of the TME and its tECM, as we believe these must be taken into account when designing therapeutic strategies. Some studies have focused on the mechanical properties of pancreatic tumours in terms of biomechanics (Maccurtain et al., 2021), viscoelasticity (Rubiano et al., 2018), and interstitial fluid mechanics (Dufort et al., 2016), which identified stiffness and tissue heterogeneity for prognosis prediction (Maccurtain et al., 2021), or suggested that viscoelastic properties can be used to more accurately distinguish between pancreatic cancer and pancreatitis (Rubiano et al., 2018). However, assessment and quantification of the architectural and chemical properties of the TME and its tECM are lacking in the literature, which could be done with a cancer biology, tissue engineering and biomaterials science interdisciplinary approach. Patient-derived tumours and their decellularized tECM are a highly biomimetic source of material for these studies, and therefore were used here (García-Gareta et al., 2022). The xenotransplantation model used provided a plentiful source of material for the present study.

Developing decellularization protocols is an intricate and time-consuming process (García-Gareta et al., 2020). An optimization study that uses factorial DOE would be very advantageous to speed up the setup of an effective protocol. DOE is a useful mathematical tool in optimization processes where several interacting factors and levels are at play (Chen et al., 2011; Levin et al., 2018; Aldawsari et al., 2022;

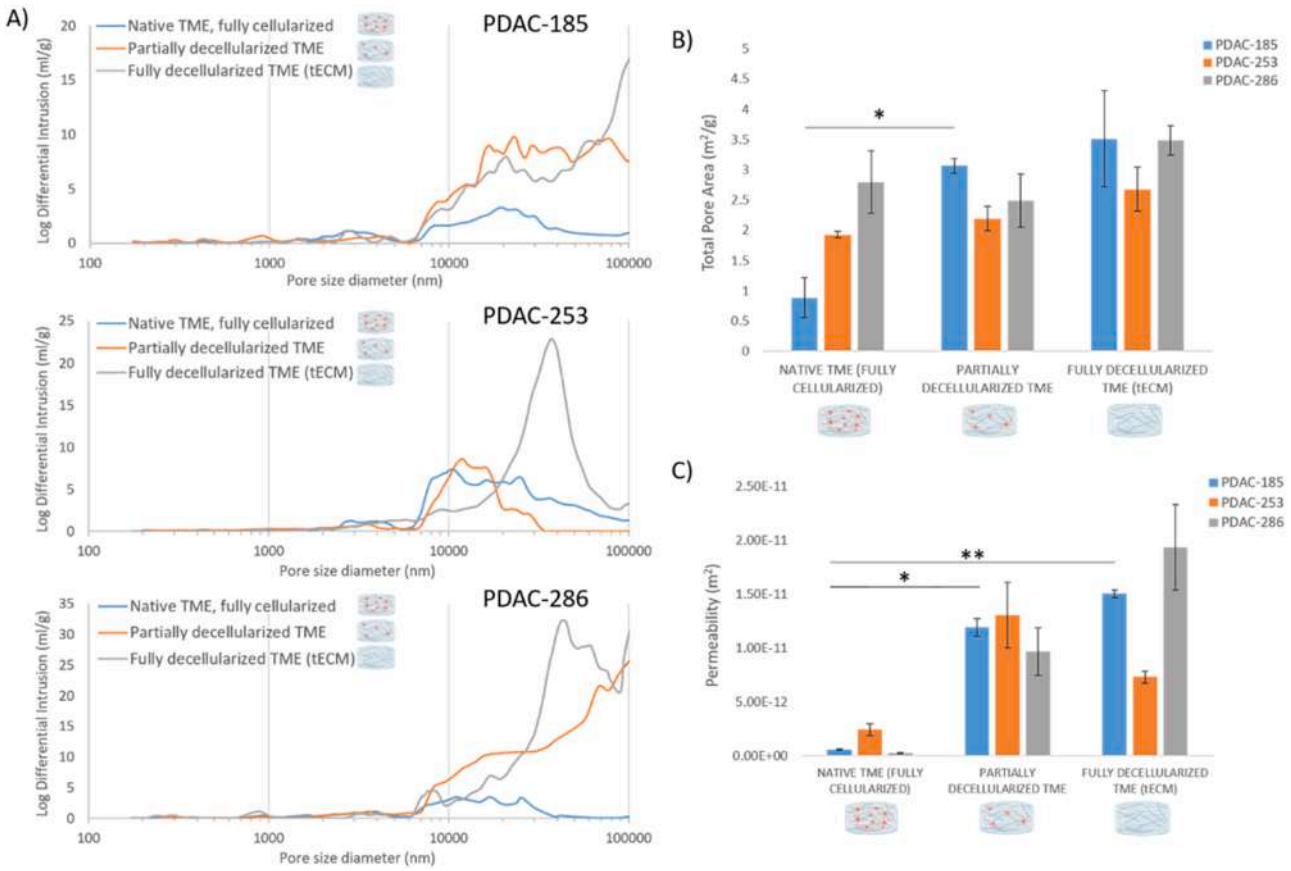

Fig. 8. MIP results for A) pore size range, B) total pore area and C) permeability. Results show mean ± standard error mean. *p < 0.05 and * *p < 0.001.

Kubit et al., 2022). Traditionally, optimization of processes in tissue engineering has been done by varying one-factor-at-a-time (OFAT) (Chen et al., 2011; Levin et al., 2018). As OFAT assumes that the different factors are independent of each other, their interaction is not studied. Moreover, OFAT experiments are time-consuming. Our factorial DOE allowed us to simultaneously vary the 3 selected factors and therefore, we could investigate their interaction to obtain a combination of parameters for effective routine decellularization of the PDAC xenografts.

Our results showed that out of the 3 factors, sonication time and number of sonication plus surfactant cycles had the greatest effect on eliminating the cells from the tumours (Fig. 3B,C). The use of ultrasounds has been shown to increase the success of decellularization in a range of different tissues and organs as ultrasounds aid in the penetration of the surfactant through the sample (Azhim et al., 2014; Syazwani et al., 2015; Forouzesh et al., 2019; Koo et al., 2021; Manalastas et al., 2021). In our study, since the native TME was so heavily populated by cells, helping the surfactant to reach the inner parts of the tumour was necessary. Adding a second sonication plus a surfactant cycle increased the effectivity of the decellularization except when a single cycle of 4 h was applied. Including an enzyme, a protease, did not have an effect on cell elimination, unless used with longer sonication times (4 h) and/or 2 cycles. Since the cellularity of the TME is so high, the amount of enzyme used did not break enough cell-tECM interactions to see an effect. Higher concentrations of enzyme could be used in the future. The most successful combination of factors was those applied in the experimental Group 6, i.e. no enzyme, and a single sonication plus surfactant cycle of 4 h, with a 99.94% reduction in cells/mm^2. On the opposite side were the conditions used in Group 4 (no enzyme, and a single sonication plus a surfactant cycle of 1 h) which yielded a 90.82% reduction in cells/mm^2. These 2 groups, along with the fully cellularized native TME, were used for validating our method as well as physico-chemical characterization of the TME and tECM.

Validation of our method showed a significant reduction in dsDNA between the native TME and the decellularized samples, which was qualitatively supported by DAPI staining of histological sections (Fig. 4). Nevertheless, results pointed towards residual trapped dsDNA left in the matrix, which would need to be eliminated before using the material for purposes like in vitro models. This could be achieved by introducing a DNase enzymatic step or further sonication plus surfactant cycles in the decellularization process (Mendibil et al., 2020; García-Gareta et al., 2022). However, we considered that the remaining dsDNA would not interfere with the physico-chemical characterization of the TME and its tECM.

Finally, we carried out biochemical assays to quantify the amount of total collagen and GAG in our experimental groups. As reported by other authors, we saw an increase in the amount of insoluble collagen with the decellularization process (Totonelli et al., 2012; Mazza et al., 2015; Maghsoudlou et al., 2016). This is a consequence of normalization by wet weight, which includes the cellular components in the native TME group, coupled with the more compact nature of the PDAC tumours (native TME) as seen by histological stainings, SEM, and MIP (Totonelli et al., 2012; Mazza et al., 2015; Maghsoudlou et al., 2016). A reduction in the amount of soluble collagen, which is not part of the ECM, was observed, which is expected since this is recently synthesized and not heavily crosslinked collagen which is soluble in neutral salt solutions like PBS (Minafra et al., 1975). However, a significant amount remained in the decellularized groups. Regarding quantification of GAG, we observed a significant reduction with decellularization, which was expected since about 30% of GAG is associated to the cell membrane (Mertens et al., 1992) and therefore, by the decellularization itself, an important fraction of GAG is eliminated (Totonelli et al., 2012; Maghsoudlou et al., 2016). However, 78.86% of GAG remained in our fully decellularized samples indicating that our optimized decellularization

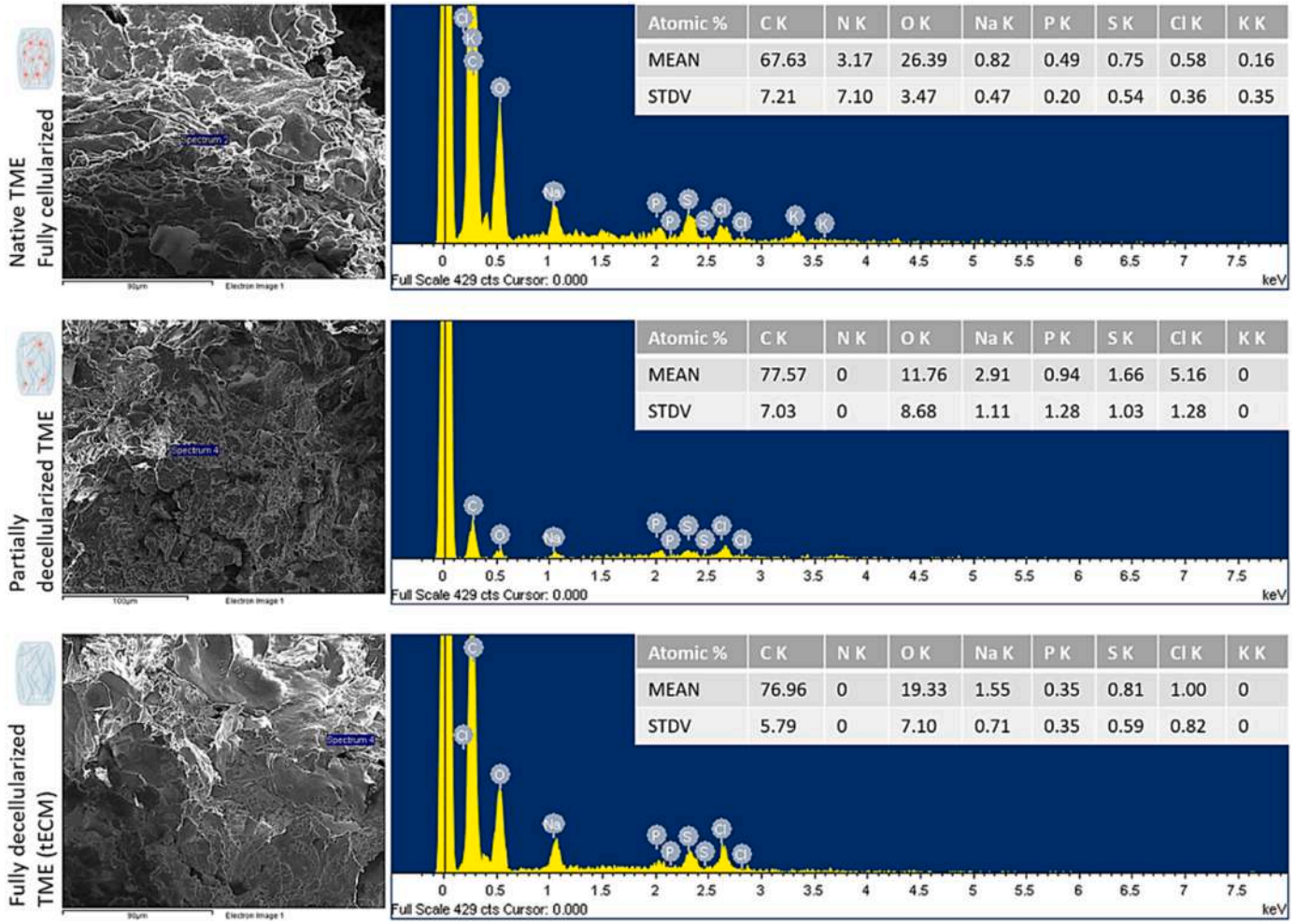

Fig. 9. Representative EDX spectra of the 3 experimental groups used for physico-chemical characterization of the TME using PDAC-185. Insert tables show the atomic percentage (mean ± standard deviation) of the different elements detected. Scale bars are 90 μm for "Native TME, fully cellularized" and "Fully decellularized TME (tECM)" groups, and 100 μm for the "Partially decellularized TME" group.

protocol retained this important component of the tECM.

The ultrasounds-based optimized protocol used in our study allowed us to address the aim of this work, namely physico-chemical assessment and quantification of the PDAC TME and its tECM. For this purpose, we performed histological stainings, SEM, pore size range quantification, total pore area and permeability assessment by MIP, elemental analysis by EDX, and molecular groups and chemical bonds analysis by FTIR. Quantifying the physico-chemical properties of the PDAC TME and its tECM is important for identifying new therapeutic targets and optimize the effectivity of existing ones.

In terms of physical properties, our SEM and MIP results showed that eliminating the cells released residual or accumulated stresses from the TME, thereby opening the porous tECM network and increasing permeability to liquids, which would make the tumour more permeable to infused drugs, large molecules, macromolecules, and cells used as therapeutic or delivery agents (Yang and Zhan, 2022). The permeability values obtained in this study are comparable to the very few reported in the literature for collagen-based scaffolds, as according to the existing literature, the tECM of PDAC is mainly composed of fibrillar collagen (Tian et al., 2021). For instance, Moreno-Arotzena and colleagues reported a permeability of $k = 1 \times 10^{-12}$ m^2 for 2 mg/ml collagen hydrogels which they calculated using a microfluidic-based experimental set-up with media columns (Moreno-Arotzena et al., 2015). Similarly, Serpooshan and co-workers reported a permeability of $k = 1 \times 10^{-12}$ to 1×10^{-14} m^2 for 1.76 mg/ml collagen gels which they theoretically calculated using Happel's model (Serpooshan et al., 2010). Without the cellular component, the tECM appears as an open network of interconnecting pores, the majority of which are in the range of 0 to 50 μm. When the cells are present, the TME displays a rather consistent appearance with a thick cell coating that would act as a barrier for therapeutic agents trying to reach the core of the tumour. Based on this observation, we would suggest initially using therapeutic agents with a diameter below 6 μm to maximize penetration into the tumour core. Taking into account that cells currently used in immune therapy, e.g. T-cell and NK cells (Waldman et al., 2020; Liu et al., 2021), have sizes of 5–8 μm (T-cells) (Chiu *et al.*, no date; Tasnim et al., 2018) and 12–15 μm (NK cells) (Chiu et al., 2019), these would mainly attack the superficial cells of the tumours, leaving the majority of cells underneath untouched. As the cellular component of the tumour is eliminated, larger therapeutic agents of up to 50 μm in diameter can be introduced. Some authors have already proposed therapies based on opening up the tECM to enhance drug permeability. For instance, Zinger and colleagues proposed using nanoparticles consisting of 100 nm liposome encapsulating collagenase (Zinger et al., 2019). These nanoparticles reduced the level of fibrotic tissue thereby allowing increased drug penetration (Zinger et al., 2019). Future work should involve confirming the pore size data presented here as well as analyzing pore interconnectivity of the TME and tECM.

Ideally, pore sizes should be measured in freshly resected samples or before resection, inside the subject. This would mean no sample

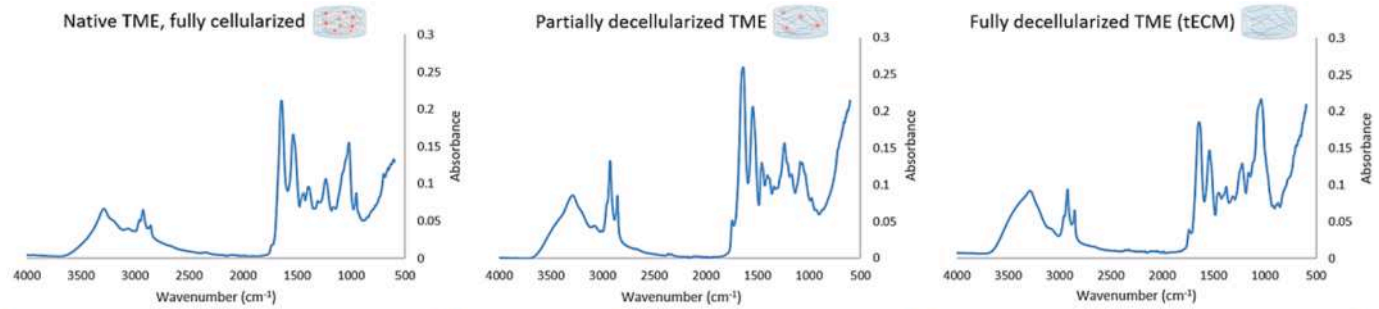

PEAK (p)/SHOULDER (s) WAVENUMBER (cm⁻¹)	ASSIGNMENT
3298.01 (p)	O-H stretch of hydroxyl groups N-H stretch, amide of proteins
3201.58 (s)	N-H stretch, amide of proteins C-H stretch, mostly proteins and lipids
3070.43 (p)	C-H stretch, mostly proteins and lipids
3022.21 (p)	C-H stretch, mostly proteins and lipids
2966.28 (p)	C-H stretch, mostly proteins and lipids
2925.78 (p)	C-H stretch, mostly proteins and lipids
2855.35 (p)	C-H stretch, mostly proteins and lipids
2846.70 (p)	C-H stretch, mostly proteins and lipids
1741.58 (s)	C=O stretch of esters
1649.01 (p)	C=O stretch, amide N-H bend, amide
1539.07 (p)	C=O stretch, amide N-H bend, amide
1517.86 (s)	**C=O stretch, amide C=C stretch of alkene groups**
1454.21 (p)	C=O stretch, amide C=C stretch of alkene groups
1442.64 (p)	C=C stretch of alkene groups
1400.21 (p)	C=C stretch of alkene groups
1367.42 (p)	C-H bend, aliphatic group
1243.99 (p)	C-H bend, aliphatic group
1195.77 (p)	C-H bend, aliphatic group C-O stretch carbohydrates and proteins
1083.91 (s)	C-O stretch carbohydrates and proteins
1054.98 (s)	C-O stretch carbohydrates and proteins
1026.05 (p)	C-O stretch carbohydrates and proteins
997.12 (p)	C-O stretch carbohydrates and proteins

Red Bold: shoulder only seen in the Control Group.
Black Bold: peaks/shoulders not seen in the Control Group.

PEAK (p)/SHOULDER (s) WAVENUMBER (cm⁻¹)	ASSIGNMENT
3419.52 (s)	**O-H stretch of hydroxyl groups**
3286.44 (p)	O-H stretch of hydroxyl groups N-H stretch, amide of proteins
3199.65 (s)	N-H stretch, amide of proteins C-H stretch, mostly proteins and lipids
3076.22 (p)	C-H stretch, mostly proteins and lipids
3010.64 (p)	C-H stretch, mostly proteins and lipids
2954.71 (s)	C-H stretch, mostly proteins and lipids
2921.92 (p)	C-H stretch, mostly proteins and lipids
2889.14 (s)	C-H stretch, mostly proteins and lipids
2854.42 (p)	C-H stretch, mostly proteins and lipids
1743.51 (p)	C=O stretch of esters
1649.00 (s)	C=O stretch, amide N-H bend, amide
1639.36 (p)	**C=O stretch, amide N-H bend, amide**
1542.93 (p)	C=O stretch, amide N-H bend, amide
1450.35 (p)	C=O stretch, amide C=C stretch of alkene groups
1396.35 (p)	C=C stretch of alkene groups
1392.49 (s)	C=C stretch of alkene groups
1344.28 (p)	**C-H bend, aliphatic group**
1328.85 (p)	**C-H bend, aliphatic group**
1282.56 (s)	**C-H bend, aliphatic group**
1230.49 (p)	C-H bend, aliphatic group
1211.20 (s)	**C-H bend, aliphatic group C-O stretch carbohydrates and proteins**
1161.05 (p)	**C-H bend, aliphatic group C-O stretch carbohydrates and proteins**
1112.84 (s)	**C-O stretch carbohydrates and proteins**
1083.91 (p)	C-O stretch carbohydrates and proteins
1076.19 (p)	C-O stretch carbohydrates and proteins
1029.91 (s)	C-O stretch carbohydrates and proteins
968.19 (p)	C-O stretch carbohydrates and proteins
918.04 (s)	**C-H out-of-plane bend of aromatic group**

PEAK (p)/SHOULDER (s) WAVENUMBER (cm⁻¹)	ASSIGNMENT
3427.23 (s)	**O-H stretch of hydroxyl groups**
3298.01 (p)	O-H stretch of hydroxyl groups N-H stretch, amide of proteins
3085.86 (s)	N-H stretch, amide of proteins C-H stretch, mostly proteins and lipids
2958.57 (s)	C-H stretch, mostly proteins and lipids
2921.92 (p)	C-H stretch, mostly proteins and lipids
2887.21 (p)	C-H stretch, mostly proteins and lipids
2854.42 (p)	C-H stretch, mostly proteins and lipids
1741.58 (p)	C=O stretch of esters
1647.08 (p)	C=O stretch, amide N-H bend, amide
1542.93 (p)	C=O stretch, amide N-H bend, amide
1467.71 (s)	**C=O stretch, amide C=C stretch of alkene groups**
1458.07 (p)	**C=O stretch, amide C=C stretch of alkene groups**
1438.78 (s)	C=C stretch of alkene groups
1411.78 (s)	C=C stretch of alkene groups
1380.92 (p)	C=C stretch of alkene groups C-H bend, aliphatic group
1319.20 (p)	**C-H bend, aliphatic group**
1247.84 (s)	C-H bend, aliphatic group
1226.63 (p)	**C-H bend, aliphatic group**
1162.98 (p)	C-H bend, aliphatic group C-O stretch carbohydrates and proteins
1116.70 (s)	**C-O stretch carbohydrates and proteins**
1062.69 (s)	C-O stretch carbohydrates and proteins
1041.48 (p)	C-O stretch carbohydrates and proteins
929.61 (p)	**C-O stretch carbohydrates and proteins C-H out-of-plane bend of aromatic group**
896.83 (p)	**C-H out-of-plane bend of aromatic group**
877.54 (p)	**C-H out-of-plane bend of aromatic group**

Fig. 10. FTIR analysis of the 3 experimental groups used for physico-chemical characterization of the TME using PDAC-185. Representative spectra are shown at the top, whilst detailed analysis of the different peaks and shoulders observed are seen in the tables below the spectra.

manipulation and/or processing and the values obtained would be essentially true to reality. A limitation of this study is that the techniques employed for obtaining pore size and permeability data require sample processing, in our case, lyophilization, which consists of freezing and drying a sample at low pressure, where ice is removed by direct sublimation (Thavornyutikarn et al., 2014). Therefore, the spaces provided by the natural pores would be filled by water, which is then frozen and subsequently sublimated leaving the original pores behind. However, collapse of the structure could occur and therefore, the specimens would be altered for subsequent measurement. With the use of MIP, the pressure arising from mercury intrusion may alter the sample's structure, or may be influenced by the swelling of the sample in the testing liquid (Bartoš et al., 2018). Furthermore, SEM is limited to 2D plane measurements in direct view and therefore, we could only access the superficial pore sizes, as indicated in the title of Section 3.6 and in Fig. 7, S3 and S4 legends (Bartoš et al., 2018). Nevertheless, SEM offers the advantage of precise visualization at very high resolutions, whilst MIP allowed us to reach the below 1 μm pores present in our samples (Bartoš et al., 2018). However, the number of nanopores measured was significantly lower compared with the number of micropores. When measuring superficial pore sizes based on SEM images, we rely on the resolution of the images themselves. With organic samples such as the ones shown here, it is a challenge to reach very high magnifications due to these materials' poor conductivity. Therefore, it is very difficult to measure pore sizes below 1 μm. With MIP, there might be some collapse of the smaller pores due to the pressure from the mercury intrusion into the porous sample. In summary, future work should involve the use of less invasive techniques that allow measurement of the pore size range reaching the nanometer scale in either fresh, or living samples, meaning inside the experimental subject. However, to the best of the authors'

knowledge, no techniques are yet available.

Regarding chemical properties, EDX showed the typical elements that are present in the molecules that comprise the tECM and cells, as well as elements coming from the chemicals used in the processing of the tumours. Some of them, e.g. sulfur, are present in both. For example, GAG are long, linear, unbranched heteropolysaccharides that mostly bear SO_3^- groups (Olson et al., 2022). GAG are a major component of the ECM of body tissues and, as shown by the Alcian blue staining (Fig. 5B), the tECM of the PDAC xenografts was very rich in GAG, which has been reported in the literature (Dufort et al., 2016).

FTIR analysis showed that the peaks/shoulders observed in the spectra correspond to organic molecular groups bonds present in proteins, lipids and carbohydrates (Malek et al., 2014; Kumar et al., 2020), as would be expected since these are the main components of the ECM of tissues (Frantz et al., 2010; Yue, 2014). As the cells are eliminated, new peaks and shoulders appeared in the spectra, the majority of which corresponded to bonds from molecular groups already detected in the native TME. The exception were the peaks (partial decellularization group) and shoulder (full decellularization group) corresponding to the C-H out-of-plane bend in aromatic groups (Margoshes and Fassel, 1955), which was not observed in the native TME: results showed that as the cells disappeared from the TME, this molecular group became accessible and therefore showed in the spectra. Thus, the availability of this group could represent a therapeutic opportunity in later stages of therapy, when the cells of the TME begin to be removed from the solid tumour. Lastly, our chemical characterization of the tumours did not suggest presence of calcification in the tECM, in agreement with the literature, which reports that calcification in PDAC is extremely rare (Lesniak et al., 2002; Ohike et al., 2008).

Coming to the end of our discussion, the main criticism of this work is the decellularization methods and sample processing used to carry out our study. Decellularization of tissues entails a fine balance between elimination of cellular content and preservation of the ECM. It is assumed that some degree of alteration is inflicted upon the matrix as the chemical and biochemical methods used to decellularize are harsh (Gilpin and Yang, 2017; García-Gareta et al., 2020). Some physical methods have been hailed as less invasive but still, alteration of the matrix is observed (Gilpin and Yang, 2017; García-Gareta et al., 2020). Likewise, as already discussed, sample processing such as lyophilization could alter the sample's structure. Therefore, results shown in this paper provide future work on two different fronts. First, the physico-chemical characterization of the PDAC TME presented here shows promising avenues for new therapeutic targets and regimes, and therefore, further in-depth characterization of the chemical and physical properties of the TME and tECM is highly recommended. To this end, alteration of samples due to processing should be minimized or eliminated. Furthermore, personalized medicine offers a powerful tool to devise therapeutic regimes tailored to the individual patient, which would provide a high likelihood of successfully treating PDAC. Our easily and cost-effectively decellularized patient-derived PDAC xenografts offer a great source material for building these models. Our group is currently working on both fronts.

5. Conclusions

In this work, we have quantified the physico-chemical properties of PDAC TME and their stroma in terms of their architecture, permeability, elemental footprint, and molecular groups/chemical bonds spectra. We observed that the PDAC TME presents an interconnected porous architecture with a very low permeability (2.25×10^{-13} – 2.44×10^{-12} m^2) and small pores (~90% of pores are lower than 10 μm). However, when the tumour is fully decellularized the permeability increases significantly (7.32×10^{-12} - 1.94×10^{-11} m^2) and also the pore size is increased (up to 82% of pores are higher than 10 μm and up to 49% pores are larger than 20 μm). This means that cellular components of the TME exert a relevant contractile role in this particular tumor, probably due to the high number of contractile-associated fibroblasts (CAFs) (Vaish et al., 2021). CAFs not only contribute to the reduction of permeability and porosity, but they are also secreting ECM proteins characteristic of desmoplastic stroma and modulating the production of cytokines/chemokines (Vaish et al., 2021). In this work, we also showed from histology that these tumors presented abundant desmoplasia with extensive protein deposition. The composition of the tECM is dominated by Carbon (C) and Oxygen (O), but Nitrogen (N) and Sulfur (S) are also present. Calcium (Ca) was not present indicating the absence of calcifications.

Overall, this research offers a potential therapeutic strategy based on the application of therapeutic agents with small size, such as drugs or therapeutic cells. Nevertheless, confirming this potential therapeutic strategy would require further work. Finally, C-H groups of aromatic groups in the tECM could also be targeted in later stages of the cancer treatment for complete elimination of tumoural components. Therefore, this work provides an original advance in our knowledge of PDAC TME from a novel perspective and opens new innovative therapeutic strategies.

Funding

This work was supported by the European Research Council (ERC) under the European Union's Horizon 2020 research and innovation programme (Advance grant agreement ICoMICS No101018587), Spanish Ministry of Economy and Competitiveness Grant No PID2021–122409OB-C21, Spanish Ministry of Science and Innovation Grant No PID2020–113819RB-I00, Government of Aragon Grant No LMP29_21, Instituto de Salud Carlos III through the Miguel Servet Program (CP16/00121 to P.S), and Fondo de Investigaciones Sanitarias (PI17/00082 and PI20/00921 to P.S) (co-financed by European funds FSE: "El FSE invierte en tu futuro" and FEDER: "Una manera de hacer Europa", respectively). E.G-G is funded by a "Ramon & Cajal Fellowship" (RYC2021–033490-I, funded by MCIN/AEI/10.13039/501100011033 and the EU "NextGenerationEU/PRTR"). P.E.G is funded by a "Margarita Salas Fellowship" (Spanish Ministry of Universities, 2021 Funding Programme for training of junior doctors). P.A-D is funded by the Government of Aragon (Grant No 2018–22).

CRediT authorship contribution statement

García-Gareta Elena: Conceptualization, Investigation, Methodology, Formal analysis, Data curation, Writing – original draft, Writing – review & editing, Resources, Supervision. **Calderón-Villalba Alejandro**: Investigation, Methodology, Writing – review & editing. **Alamán-Díez Pilar**: Investigation, Methodology, Formal analysis. **Gracia Costa Carlos**: Investigation, Formal analysis. **Enrique Guerrero Pedro**: Investigation, Methodology. **Mur Carlota**: Investigation, Methodology. **Rueda Flores Ana**: Investigation, Formal analysis. **Olivera Jurjo Nerea**: Investigation, Formal analysis. **Sancho Patricia**: Methodology, Resources, Writing – review & editing. Pérez María Ángeles: Resources, Writing – review & editing. **García-Aznar José Manuel**: Conceptualization, Project administration, Resources, Supervision, Writing – review & editing.

Declaration of Competing Interest

The authors declare that the research was conducted in the absence of any commercial or financial relationships that could be construed as a potential conflict of interest.

Data availability

Data will be made available on request.

Acknowledgments

The authors would like to thank Nuria Navascués from the Aragon Institute of Nanoscience & Materials (INMA, Zaragoza, Aragon, Spain) for technical support with FTIR, Marta Navarro and Gala Simón from the Laboratory of Advanced Microscopies at INMA (Zaragoza, Aragon, Spain) for technical support with SEM and EDX, Cindy Giraldo from the Anatomical Pathology Service at Aragon Institute of Health Sciences (IACS, Zaragoza, Aragon, Spain) for histological processing and staining of samples, and Patricia Ugarte and Miguel Menéndez from the Aragon Institute of Engineering Research (I3A, Zaragoza, Aragon, Spain) for technical support with MIP and useful discussions. We also acknowledge the use of the Animal Facility at IACS-University of Zaragoza and Servicio General de Apoyo a la Investigación-SAI, University of Zaragoza.

Appendix A. Supporting information

Supplementary data associated with this article can be found in the online version at doi:10.1016/j.ejcb.2024.151396.

References

Aldawsari, H.M., et al., 2022. Surface-tailoring of emulsomes for boosting brain delivery of vinpocetine via intranasal route: in vitro optimization and in vivo pharmacokinetic assessment (Available at:). Drug Deliv. 29 (1), 2671–2684. https://doi.org/10.1080/10717544.2022.2110996.

Azhim, A., et al., 2014. The use of sonication treatment to decellularize aortic tissues for preparation of bioscaffolds (Available at:). J. Biomater. Appl. 29 (1), 130–141. https://doi.org/10.1177/0885328213517579.

Bartoš, M., Suchý, T., Foltán, R., 2018. Note on the use of different approaches to determine the pore sizes of tissue engineering scaffolds: what do we measure? (Available at:). Biomed. Eng. Online 17 (1). https://doi.org/10.1186/s12938-018-0543-z.

Bengtsson, A., Andersson, R., Ansari, D., 2020. The actual 5-year survivors of pancreatic ductal adenocarcinoma based on real-world data (Available at:). Sci. Rep. 10, 16425. https://doi.org/10.1038/s41598-020-73525-y.

Chen, Y., et al., 2011. Characterization and optimization of cell seeding in scaffolds by factorial design: quality by design approach for skeletal tissue engineering (Available at:). Tissue Eng. Part C: Methods 17 (12), 1211–1221. https://doi.org/10.1089/ten.tec.2011.0092.

Chiu, P.-L. et al. (2019) 'Rapid and safe Isolation of Human peripheral Blood B and t Lymphocytes through spiral Microfluidic Channels'. Available at: https://doi.org/10.1038/s41598–019-44677–3.

Cozzi, E., et al., 2009. Xenotransplantation as a model of integrated, multidisciplinary research (Available at:). Organogenesis 5 (1), 288–296. https://doi.org/10.4161/org.7578.

Dufort, C.C., Delgiorno, K.E., Hingorani, S.R., 2016. Mounting pressure in the microenvironment: fluids, solids, and cells in pancreatic ductal adenocarcinoma (Available at:). *Gastroenterol.* W. B. Saunders 1545–1557.e2. https://doi.org/10.1053/j.gastro.2016.03.040.

Feig, C., et al., 2012. The pancreas cancer microenvironment tumor microenvironment-achilles' heel of pancreatic cancer?' (Available at:). Clin. Cancer Res. 18 (16). https://doi.org/10.1158/1078-0432.CCR-11-3114.

Forouzesh, F., Rabbani, M., Bonakdar, S., 2019. A comparison between ultrasonic bath and direct sonicator on osteochondral tissue decellularization (Available at:). J. Med. Signals Sens. 9 (4), 227–233. https://doi.org/10.4103/jmss.JMSS_64_18.

Frantz, C., Stewart, K.M., Weaver, V.M., 2010. The extracellular matrix at a glance (Available at:). J. Cell Sci. 123 (24), 4195. https://doi.org/10.1242/jcs.023820.

García-Gareta, E. *et al.* (2020) 'Decellularised scaffolds: just a framework? Current knowledge and future directions', Journal of Tissue Engineering. SAGE Publications Ltd. Available at: https://doi.org/10.1177/2041731420942903.

García-Gareta, E., Pérez, M.Á. and García-Aznar, J.M. (2022) 'Decellularization of tumours: A new frontier in tissue engineering', Journal of Tissue Engineering. SAGE Publications Ltd. Available at: https://doi.org/10.1177/20417314221091682.

Gilpin, A. and Yang, Y. (2017) 'Decellularization Strategies for Regenerative Medicine: From Processing Techniques to Applications', BioMed Research International. Edited by C. Del Gaudio, 2017, p. 9831534. Available at: https://doi.org/10.1155/2017/9831534.

Hassan, D.H., et al., 2022. Compritol-based nanostrucutured lipid carriers (NLCs) for augmentation of zolmitriptan bioavailability via the transdermal route: in vitro optimization, ex vivo permeation, in vivo pharmacokinetic study (Available at:). Pharmaceutics 14 (7), 1484. https://doi.org/10.3390/pharmaceutics14071484.

Henke, E., Nandigama, R. and Ergün, S. (2020) 'Extracellular Matrix in the Tumor Microenvironment and Its Impact on Cancer Therapy', Frontiers in Molecular Biosciences. Frontiers Media S.A. Available at: https://doi.org/10.3389/fmolb.2019.00160.

Hoffmann, N. *et al.* (2020) 'A Xenotransplant Model of Human Brain Tumors in Wild-Type Mice', iScience. 2019/12/30, 23(1), p. 100813. Available at: https://doi.org/10.1016/j.isci.2019.100813.

Hoshiba, T., 2019. Decellularized extracellular matrix for cancer research (Available at:). Materials 12 (8), 1311. https://doi.org/10.3390/ma12081311.

Kim, P.K., et al., 2021. Hyaluronic acid fuels pancreatic cancer cell growth (Available at:). eLife 10. https://doi.org/10.7554/eLife.62645.

Koo, M.-A., et al., 2021. Preconditioning process for dermal tissue decellularization using electroporation with sonication (Available at:). Regen. Biomater. 9. https://doi.org/10.1093/rb/rbab071.

Kubit, A., et al., 2022. Multi-criteria optimisation of friction stir welding parameters for EN AW-2024-T3 aluminium alloy joints (Available at:). Materials 15 (15), 5428. https://doi.org/10.3390/ma15155428.

Kulkarni, N.S., et al., 2022. Development of gelatin methacrylate (GelMa) hydrogels for versatile intracavitary applications (Available at:). Biomater. Sci. 10 (16), 4492–4507. https://doi.org/10.1039/D2BM00022A.

Kumar, V., Asodiya, F.A., Kumar, N., 2020. Fourier Transform Infrared Spectroscopy of the Animal Tissues. In: Vora, S.D. (Ed.), Real Perspective of Fourier Transforms and Current Developments in Superconductivity. IntechOpen, Rijeka. https://doi.org/10.5772/intechopen.94582.

Lesniak, R.J., Hohenwalter, M.D., Taylor, A.J., 2002. Spectrum of causes of pancreatic calcifications. Am. J. Roentgenol. 178, 79–86.

Levin, A. *et al.* (2018) 'The importance of factorial design in tissue engineering and biomaterials science: Optimisation of cell seeding efficiency on dermal scaffolds as a case study', Journal of Tissue Engineering, 9, p. 204173141878169. Available at: https://doi.org/10.1177/2041731418781696.

Liu, S. *et al.* (2021) 'NK cell-based cancer immunotherapy: from basic biology to clinical development', Journal of Hematology and Oncology. BioMed Central Ltd. Available at: https://doi.org/10.1186/s13045–020-01014-w.

Lü, W.-D., et al., 2014. Development of an acellular tumor extracellular matrix as a three-dimensional scaffold for tumor engineering (Available at:). PloS One 9 (7). https://doi.org/10.1371/journal.pone.0103672.

Maccurtain, B.M., et al., 2021. Clinical medicine pancreatic ductal adenocarcinoma: relating biomechanics and prognosis (Available at:). J. Clin. Med 10, 2711. https://doi.org/10.3390/jcm10122711.

Maghsoudlou, P., et al., 2016. Optimization of liver decellularization maintains extracellular matrix micro-architecture and composition predisposing to effective cell seeding (Available at:). PLOS ONE 11 (5), e0155324. https://doi.org/10.1371/journal.pone.0155324.

Malek, K., Wood, B.R., Bambery, K.R., 2014. FTIR Imaging of Tissues: Techniques and Methods of Analysis. In: Baranska, M. (Ed.), Optical Spectroscopy and Computational Methods in Biology and Medicine. Springer Netherlands, Dordrecht, pp. 419–473. https://doi.org/10.1007/978-94-007-7832-0_15.

Malekpour, Z., et al., 2021. Preparation and characterization of poly (lactic-co-glycolic acid) nanofibers containing simvastatin coated with hyaluronic acid for using in periodontal tissue engineering (Available at:). Biotechnol. Prog. 37 (6). https://doi.org/10.1002/btpr.3195.

Manalastas, T.M., et al., 2021. Effect of decellularization parameters on the efficient production of kidney Bioscaffolds (Available at:). Appl. Biochem. Biotechnol. 193 (5), 1239–1251. https://doi.org/10.1007/s12010-020-03338-2.

Margoshes, M., Fassel, V.A., 1955. The infrared spectra of aromatic compounds: I. The out-of-plane C-H bending vibrations in the region 625–900 cm−1′ (Available at:). Spectrochim. Acta 7 (C), 14–24. https://doi.org/10.1016/0371-1951(55)80003-3.

Matossian, M.D., et al., 2018. A novel patient-derived xenograft model for claudin-low triple-negative breast cancer (Available at:). Breast Cancer Res. Treat. 169 (2), 381–390. https://doi.org/10.1007/s10549-018-4685-2.

Mazza, G., et al., 2015. Decellularized human liver as a natural 3D-scaffold for liver bioengineering and transplantation (Available at:). Sci. Rep. 5 (1), 13079. https://doi.org/10.1038/srep13079.

Mendibil, U., et al., 2020. Tissue-specific decellularization methods: rationale and strategies to achieve regenerative compounds (Available at:). Int. J. Mol. Sci. 1–29. https://doi.org/10.3390/ijms21155447.

Mertens, G., et al., 1992. Cell surface heparan sulfate proteoglycans from human vascular endothelial cells. Core protein characterization and antithrombin III binding properties (Available at:). J. Biol. Chem. 267 (28), 20435–20443. https://doi.org/10.1016/S0021-9258(19)88721-5.

Minafra, S., et al., 1975. Chromatographic characterization of soluble collagen in sea urchin embryos (Paracentrotus lividus) (Available at:). Bolletino di Zool. 42 (2–3), 205–208. https://doi.org/10.1080/11250007509431430.

Moreno-Arotzena, O., et al., 2015. Characterization of fibrin and collagen gels for engineering wound healing models (Available at:). Materials 8 (4), 1636–1651. https://doi.org/10.3390/ma8041636.

Nazim, V.S. *et al.* (2022) 'Functionalized SnO2 nanoparticles with gallic acid via green chemical approach for enhanced photocatalytic degradation of citalopram: synthesis, characterization and application to pharmaceutical wastewater treatment', Environmental Science and Pollution Research [Preprint]. Available at: https://doi.org/10.1007/s11356–022-22447–5.

Ohike, N. *et al.* (2008) Ductal Adenocarcinoma of the Pancreas with Psammomatous Calcification. Report of a Case, JOP. Journal of the Pancreas. Available at: http://www.joplink.net.

Olson, K.R., et al., 2022. Heparan sulfate, mucopolysaccharidosis iiib and sulfur metabolism disorders (Available at:). Antioxidants 11 (4), 678. https://doi.org/10.3390/antiox11040678.

Ricci, C., Moroni, L., Danti, S., 2013. Cancer tissue engineering new perspectives in understanding the biology of solid tumours a critical review (Available at:). OA Tissue Eng. 1 (1). https://doi.org/10.13172/2052-9643-1-1-607.

Rubiano, A., et al., 2018. Viscoelastic properties of human pancreatic tumors and in vitro constructs to mimic mechanical properties (Available at:). Acta Biomater. 67, 331–340. https://doi.org/10.1016/j.actbio.2017.11.037.

Sampson, K., et al., 2021. Cultivation of hierarchical 3D scaffolds inside a perfusion bioreactor: scaffold design and finite-element analysis of fluid flow (Available at:). SN Appl. Sci. 3 (12). https://doi.org/10.1007/s42452-021-04871-3.

Sarantis, P., et al., 2020. Pancreatic ductal adenocarcinoma: treatment hurdles, tumor microenvironment and immunotherapy Open-Access (Available at:). World J. Gastrointest. Oncol. 12 (2), 173–181. https://doi.org/10.4251/wjgo.v12.i2.173.

Schober, M., et al., 2014. Desmoplasia and chemoresistance in pancreatic cancer (Available at:). Cancers 2137–2154. https://doi.org/10.3390/cancers6042137.

Serpooshan, V., et al., 2010. Reduced hydraulic permeability of three-dimensional collagen scaffolds attenuates gel contraction and promotes the growth and differentiation of mesenchymal stem cells (Available at:). Acta Biomater. 6 (10), 3978–3987. https://doi.org/10.1016/j.actbio.2010.04.028.

Syazwani, N., et al., 2015. Decellularization of aorta tissue using sonication treatment as potential scaffold for vascular tissue engineering (Available at:). J. Med. Biol. Eng. 35 (2), 258–269. https://doi.org/10.1007/s40846-015-0028-5.

Tasnim, H., et al., 2018. Quantitative measurement of Naïve T cell association with dendritic cells, FRCs, and blood vessels in lymph nodes (Available at:). Front. Immunol. 9 (JUL). https://doi.org/10.3389/fimmu.2018.01571.

Thavornyutikarn, B., et al., 2014. Bone tissue engineering scaffolding: computer-aided scaffolding techniques (Available at:). Prog. Biomater. 3 (2), 61–102. https://doi.org/10.1007/s40204-014-0026-7.

Tian, C., et al., 2021. Suppression of pancreatic ductal adenocarcinoma growth and metastasis by fibrillar collagens produced selectively by tumor cells (Available at:). Nat. Commun. 12 (1). https://doi.org/10.1038/s41467-021-22490-9.

Totonelli, G., et al., 2012. A rat decellularized small bowel scaffold that preserves villus-crypt architecture for intestinal regeneration (Available at:). Biomaterials 33 (12), 3401–3410. https://doi.org/10.1016/j.biomaterials.2012.01.012.

Vaish, U. *et al.* (2021) 'Cancer-associated fibroblasts in pancreatic ductal adenocarcinoma: An update on heterogeneity and therapeutic targeting', International Journal of Molecular Sciences. MDPI. Available at: https://doi.org/10.3390/ijms222413408.

Waldman, A.D., Fritz, J.M. and Lenardo, M.J. (2020) 'A guide to cancer immunotherapy: from T cell basic science to clinical practice'. Available at: https://doi.org/10.1038/s41577–020-0306–5.

Whatcott, C.J., et al., 2015. Desmoplasia in Primary Tumors and Metastatic Lesions of Pancreatic Cancer (Available at:). Clin. Cancer Res.: Off. J. Am. Assoc. Cancer Res. 21 (15), 3561–3568. https://doi.org/10.1158/1078-0432.CCR-14-1051.

Winkler, J., et al., 2020. Concepts of extracellular matrix remodelling in tumour progression and metastasis (Available at:). Nat. Commun. 11 (1), 5120. https://doi.org/10.1038/s41467-020-18794-x.

Yang, Y., Zhan, W., 2022. Role of tissue hydraulic permeability in convection-enhanced delivery of nanoparticle-encapsulated chemotherapy drugs to brain tumour (Available at:). Pharm. Res. 39 (5), 877–892. https://doi.org/10.1007/s11095-022-03261-7.

Yue, B., 2014. Biology of the extracellular matrix: an overview (Available at:). J. Glaucoma 23 (8 Suppl 1), S20–S23. https://doi.org/10.1097/IJG.0000000000000108.

Zinger, A., et al., 2019. Collagenase nanoparticles enhance the penetration of drugs into pancreatic tumors (Available at:). ACS Nano 13, 11008–11021. https://doi.org/10.1021/acsnano.9b02395.